optica

Single-chip nanophotonic near-field imager: supplementary material

FARSHID ASHTIANI,* ANGELINA RISI, AND FIROOZ AFLATOUNI

Department of Electrical and Systems Engineering, University of Pennsylvania, Philadelphia, PA 19104, USA
**Corresponding author: farshid@seas.upenn.edu*

Published 26 September 2019

This document provides supplementary information to "Single-chip nanophotonic near-field imager," https://doi.org/10.1364/OPTICA.6.001255.

1. Supplementary Note S1: An optically delayed electrical pulse

One of the main concepts in the design of the integrated nanophotonic near-field imager is that an electrical pulse can be delayed optically. In this case, an optical signal is first modulated by the input electrical signal, delayed using a true-time-delay (TTD) cell, and photo-detected to recover the delayed version of the input electrical signal. Here we consider this effect for two typical cases, where the electro-optical conversion is performed using either a Mach Zehnder modulator (MZM) or a ring modulator.

Figure S1(a) shows the block diagram of the system that optically delays an electrical signal with a MZM as the intensity modulator. Consider the case that the electric field of the optical wave in the form of $E_L = \sqrt{P_0}e^{j(\omega_0 t)}$ is modulated with the input radio frequency (RF) signal $V_{RF} = v_0\cos(\omega_{RF}t)$ using the MZM. When the phase difference between the two arms of the MZM, θ, is set to 90°, the electric field of the modulated optical signal is written as $E_o = \frac{1}{2}e^{j\omega_0 t}\{j\sqrt{P_0} + \sqrt{P_1}e^{j\left(\frac{\pi}{V_\pi}V_{RF}(t)\right)}\}$, where P_0, P_1, ω_0, v_0, ω_{RF}, and V_π are the laser power (before the modulator), the light power after the phase modulator (in the top branch of the MZM), the laser frequency, the RF signal amplitude, the RF signal frequency, and the modulator phase-to-voltage gain, respectively. The modulated signal is delayed using an optical TTD cell with a delay of τ_o. The resulting electric field of the delayed optical signal is written as $E_D = \frac{1}{2}e^{j\omega_0(t-\tau_o)}\{j\sqrt{P_0} + \sqrt{P_1}e^{j\left(\frac{\pi}{V_\pi}v_0\cos[\omega_{RF}(t-\tau_o)]\right)}\}$. The delay line output is photo-detected and the photo-current is written as $i_{RF,out} = \frac{1}{4}R\{P_0 + P_1 + 2\sqrt{P_0P_1}\sin\left[\left(\frac{v_0}{V_\pi}\right)\cos\left(\omega_{RF}(t-\tau_o)\right)\right]\}$, where R represents the photodiode responsivity. In this case, using the Jacobi-Anger expansion [1] the fundamental component of the photo-current is written as $i_{RF,out} \approx R\sqrt{P_0P_1}J_1\left(\frac{v_0}{V_\pi}\right)\cos(\omega_{RF}(t-\tau_o))$ indicating that the electrical signal is delayed by the amount of the delay of the optical TTD element. Note that J_1 denotes the Bessel function of the first kind.

Figure S1(b) shows the block diagram of the system that optically delays an electrical signal using a ring modulator. Consider the case that the electric field of the optical wave in the form of $E_L = \sqrt{P_0}e^{j(\omega_0 t)}$ is modulated with the input RF signal $V_{RF} = v_0\cos(\omega_{RF}t)$ using a ring modulator. The applied RF signal perturbs the index of refraction of the ring structure [2], that is, $n(t) = n + \Delta n\cos(\omega_{RF}t)$, where n is the constant (un-perturbed) index and $\Delta n = \frac{\lambda_0}{2L}\left(\frac{v_0}{V_\pi}\right)$ is the amplitude of index change due to the applied RF signal, and λ_0, L and V_π are the laser wavelength in free-space, the effective length of the phase modulator in the ring, and the phase-to-voltage gain, respectively. In this case, the instantaneous output power of the ring modulator can be approximated as [2]

$$P_o = P_1 + H_n(\omega_{RF})\Delta n\cos(\omega_{RF}t + \phi), \qquad \textbf{(S1)}$$

where P_1 is the constant part of the output optical power, ϕ is the phase of the small-signal instantaneous output power, and $H_n(\omega_{RF}) = \frac{\Delta p}{\Delta n}$ is the linearized transfer function as the ratio of the output power perturbation to the small-signal index perturbation, which can be written as [2]

$$H_n(\omega_{RF}) = P_{in}\left[\frac{\omega_r}{n}\times\frac{2\delta}{\delta^2+\frac{1}{4\tau^2}}\times\frac{k_e^2}{T}\times\frac{j\omega_{RF}+\frac{1}{2\tau}}{(j\omega_{RF})^2+j\frac{\omega_{RF}}{\tau}+\frac{1}{4\tau^2}+\delta^2}\right], \qquad \textbf{(S2)}$$

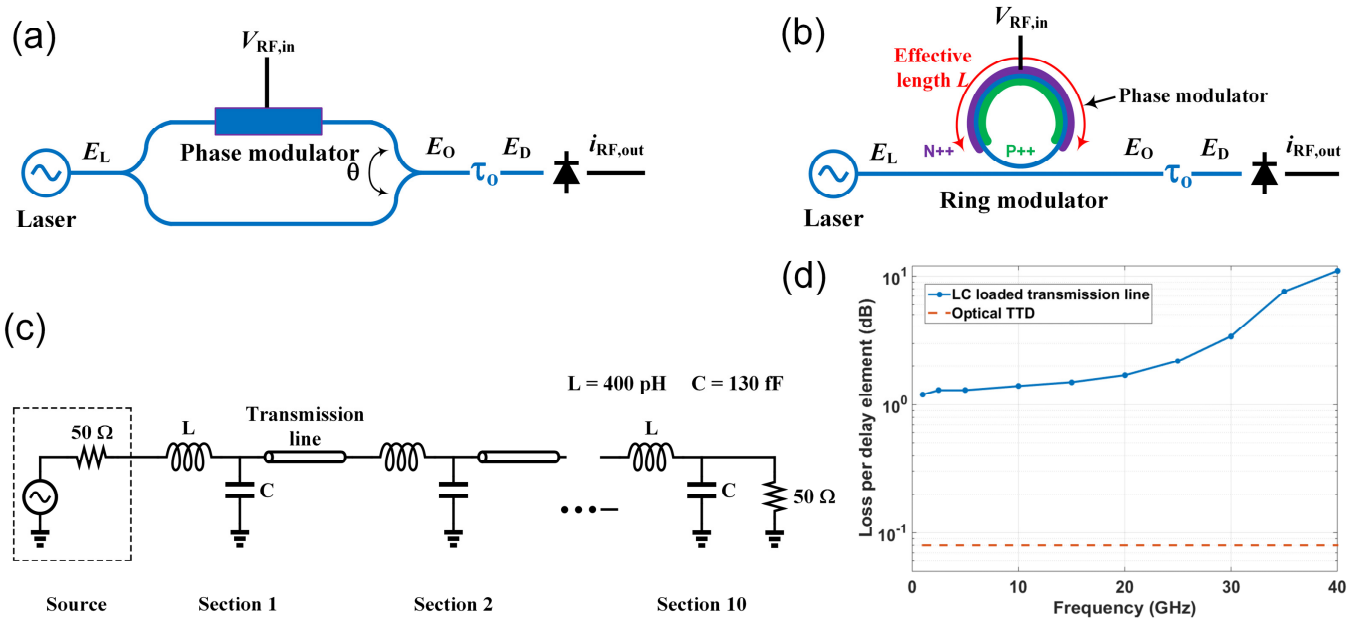

Fig. S1. Optically delayed electrical pulse and comparison of optical and electrical delay lines. (a) Optically delayed electrical signal using a MZM. (b) Optically delayed electrical signal using a ring modulator. In both a and b, the modulator is followed by a delay cell to optically delay the electrical signal $V_{RF,in}$. (c) Schematic of a loaded transmission line with LC segments. Each transmission line segment is 250 µm long and the inductor and capacitor values are 400 pH and 130 fF, respectively. (d) Comparison between the simulated per-delay element loss of the implemented optical delay and that of the LC loaded transmission line for the same delay of 9.8 ps.

where ω_r, τ, $\delta = \omega_0 - \omega_r$, ω_0, k_e, and T are the resonance frequency of the ring, the photon lifetime, the difference between the input laser frequency and the ring resonance frequency, the frequency of the input laser, the coupling coefficient of the ring modulator, and the round trip time of the ring, respectively. Equation S2 indicates that in presence of an input optical wave and a known modulating RF signal, $H_n(\omega_{RF})$ is a constant and therefore, based on Equation S1, the time varying part of the output power is only proportional to $\cos(\omega_{RF}t)$. The modulator output is delayed using an optical TTD cell with delay of τ_o and photo-detected using a photodiode with responsivity of R. In this case, the AC component of the photo-current is written as

$$i_{RF,out} \approx RH_n(\omega_{RF})\frac{\lambda_0}{2L}\left(\frac{1}{V_\pi}\right)v_0\cos[\omega_{RF}(t-\tau_o)+\phi], \qquad \textbf{(S3)}$$

indicating that the electrical signal is delayed by the amount of the delay of the optical TTD element.

Comparison of electrical and optical delay lines - Conventionally, the all-electrical on-chip delay lines are implemented either by setting the length of a transmission line [3] or periodically loading a transmission line with series inductors and shunt capacitors (LC segments) to change the propagation velocity [4]. In both methods, the loss of the silicon substrate introduces a large propagation loss for the on-chip delay lines [5]. For imagers with small number of delay lines, repeating amplifiers (or line amplifiers) may be used [6] to compensate for the loss of the delay line at the cost of high power consumption, excess noise, and reduced bandwidth, and delay non-uniformity. In addition, the long transmission line per delay element (due to the high propagation velocity) in the former method, and the large size of the inductors in the latter method result in a large per delay line chip area. The resulting large area and high power consumption of the on-chip electrical delay lines as well as sensitivity to magnetic coupling and vulnerability to electromagnetic interference significantly limit the scalability of on-chip near-field imagers implemented on standard electronic processes. Between the two aforementioned design methods for electrical TTD elements, the second method is often preferred [6] as it provides an overall smaller delay element size. Note that the loss of the LC segments (or transmission lines) increases with frequency while that of the optical TTD remains constant across a large frequency range.

Figure S1(c) shows the schematic of an integrated all-electrical delay line implemented using a loaded transmission line with LC segments. Figure S1(d) shows the simulated loss per delay cell of the structure in Fig. S1(c), implemented using top two metal layers (4 µm thick aluminum and 0.5 µm thick copper) in a standard 90 nm RF CMOS SOI process with 7 metal layers, which is compared with the loss of the optical TTD element, implemented on IME silicon-on-insulator process, for the same delay of 9.8 ps. As expected, for the same delay, the loss of the optical delay line is significantly lower than that of the LC loaded transmission line. Furthermore, the loss of the LC loaded transmission line increases with frequency while that of the optical delay line remains unchanged. At 2.5 GHz and 35 GHz, the loss of the optical delay line is 16 times and 100 times lower than that of the electrical delay line, respectively.

2. Supplementary Note S2: 1-D delay line array design

In the reported nanophotonic near-field imager, it is necessary for the output of each of the four ring modulators to be equally distributed among all 121 pixels to form a uniform image. In the proposed imager, first, two 1-D delay line arrays equally distribute the light among 11 columns (Fig. 2(b) of the paper), and then, the same 1-D delay line array is used in each column to equally distribute the light

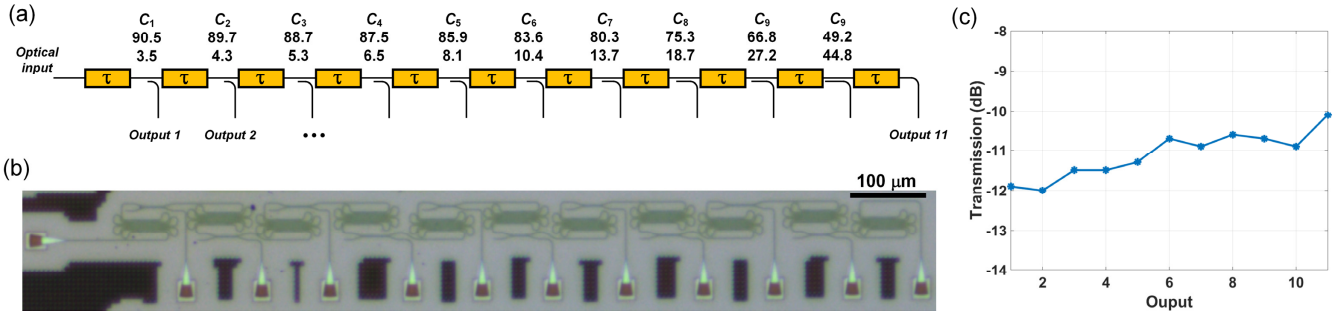

Fig. S2. 1-D delay line array. (a) Schematic of the delay line array with 11 outputs with the required coupling ratios that are chosen based on simulation results. (b) The microphotograph of the 1-D delay line array. (c) The measured optical power at the 11 outputs.

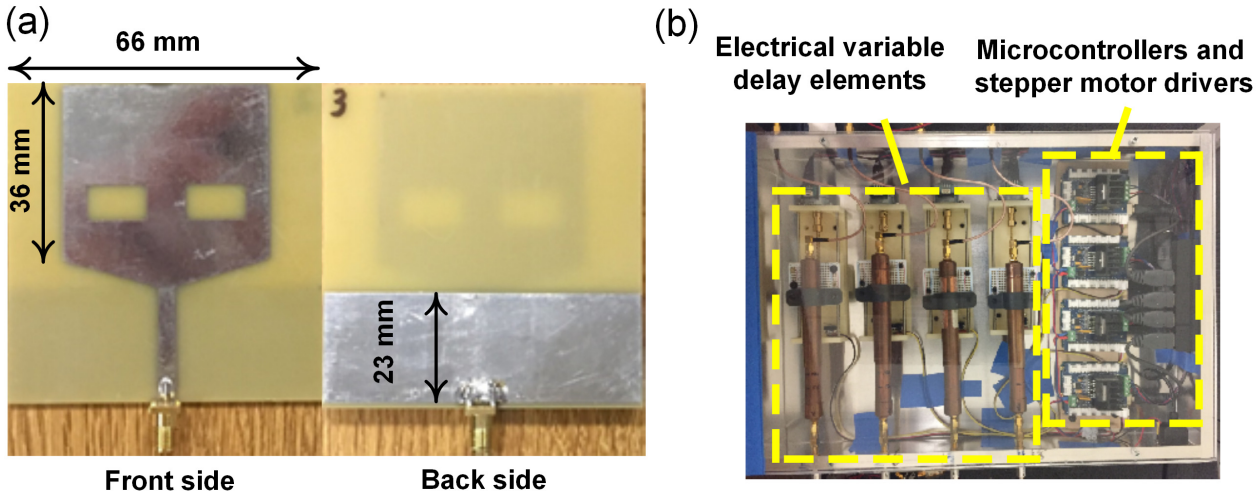

Fig. S3. UWB antenna and electrical variable delay line. (a) Fabricated UWB antenna. (b) 4-channel wideband electrical variable delay line system.

among 11 photodiodes. The structure of the 1-D delay line array is shown in Fig. S2(a), where a directional coupler is placed after each delay line. To achieve equal power distribution, the required coupling ratio for each directional coupler is calculated. Note that the directional couplers as well as the delay elements have non-ideal (less than 100%) transmission coefficient. For each coupler in Fig. S2(a), the top number denotes the percentage of the power guided to the next delay cell and the bottom number shows the amount of power coupled to the ith output (C_i represents the ith coupler). These coupling ratios are realized by adjusting the coupling length and spacing for each directional coupler. Figure S2(b) shows the microphotograph of the 1-D delay line array which was separately implemented on the same IME silicon-on-insulator run. The characterization result is shown in Fig. S2(c), where less than 2 dB variation across the 11 outputs is observed.

3. Supplementary Note S3: UWB antenna and variable delay line design

In order to perform wireless measurements and imaging, four wideband antennas are used to form the 2x2 receive antenna array. The incoming signal is a monocycle pulse whose frequency spectrum covers a range of about 500 MHz to 5 GHz. Therefore, the bandwidth of these antennas should be large enough to preserve the shape of the pulse. The antenna used in this implementation is based on the knight's helm design [7] optimized for operation in the 500 MHz to 5GHz range. Figure S3(a) shows the fabricated antenna implemented on a FR4 printed circuit board.

In the wired measurement setup in Fig. 3(a) of the paper, the output of the pulse generator is connected to four wideband electrical variable delay lines to emulate UWB signals impinging from different directions. Figure S3(b) shows the implemented 4-channel variable delay line system that can be mechanically adjusted using stepper motors. This system provides a per-channel delay range of 0 to 220 ps with a resolution of 0.06 ps and an insertion loss of less than 2 dB across the bandwidth of interest.

4. Supplementary Note S4: Coherence effect on image SNR

In the implemented nanophotonic near-field imager, for a given angle of incidence of the impinging UWB pulse, all four modulated optical waves will arrive at the same time at a certain pixel, where they are combined and photo-detected. Since all four modulated optical waves are originated from the same laser, their constructive addition at the combining point depends on their instantaneous relative phases. Therefore, phase mismatches between these four optical waves, as a result of fabrication process variations, thermal gradient across the chip, or other effects, may affect their constructive addition lowering the detection SNR. Figure S4 shows the block diagram of our proposed scheme to address this issue. The laser source is frequency chirped and coupled to the chip. The coupled light is split into four

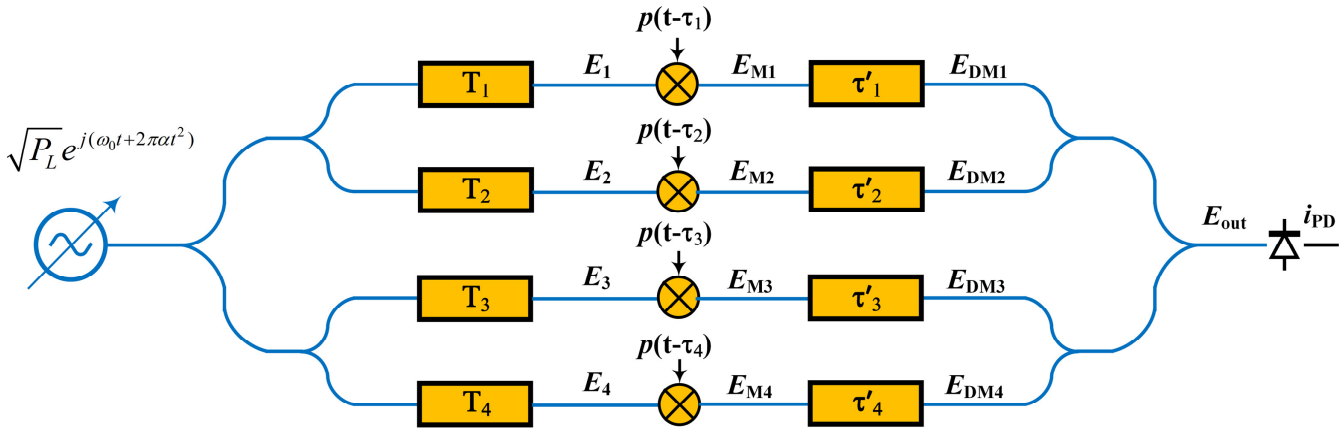

Fig. S4. Proposed scheme to address the potential phase mismatch between optical waves at the combining point before each pixel.

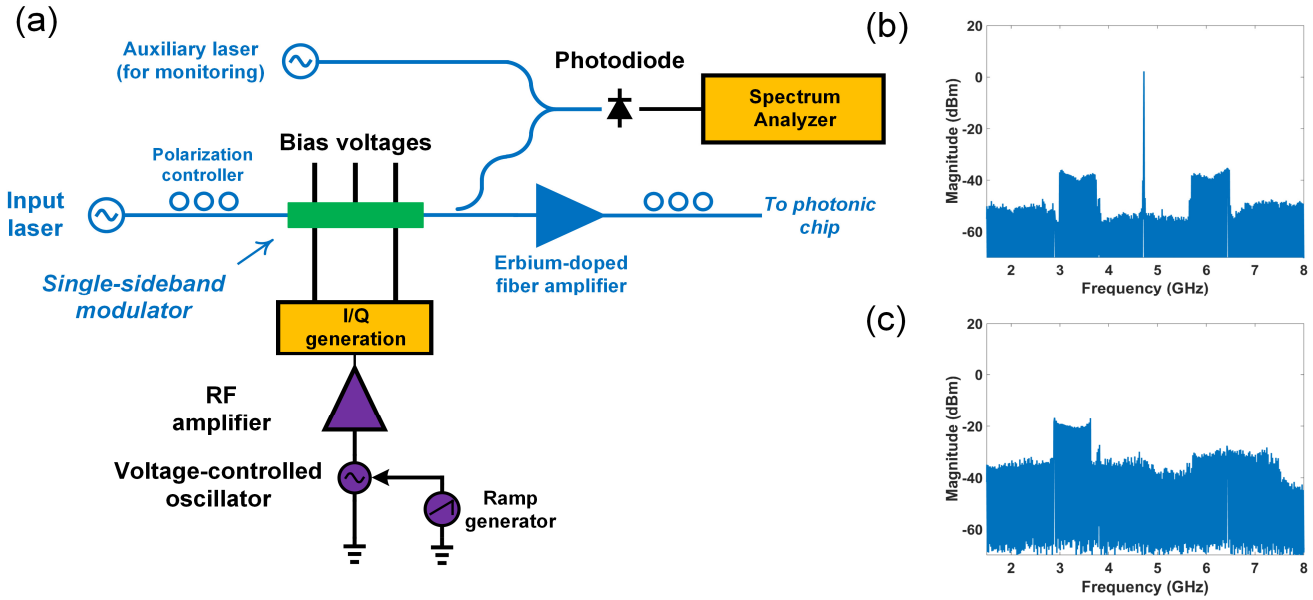

Fig. S5. Chirp generation. (a) Block diagram of the laser frequency chirp generation system. (b) Spectrum of the optical signal with zero modulator bias and, (c) with single-sideband operation biasing condition, where the optical carrier and the undesired sideband are significantly suppressed. The frequency spectrum of the laser is down-converted using an auxiliary laser.

branches and guided to the four ring modulators using waveguides with different lengths (corresponding to four different delays of T_1 to T_4).

Consider the case that the laser output electric field after frequency chirping is written as $E_L(t) = \sqrt{P_L}e^{j(\omega_0 t+2\pi\alpha t^2)}$, where P_L, ω_0 and α are the laser power, the laser frequency, and the laser frequency chirp rate, respectively. The electric field of the light in the i^{th} branch (i =1, 2, 3, 4) after the delay line (right before the ring modulator) is written as $E_i(t) = \sqrt{P_0}e^{j(\omega_i t+\phi_i)}$, where $\omega_i = \omega_0 - 4\pi\alpha T_i + 2\pi\alpha t$, $\phi_i = 2\pi\alpha T_i^2 - \omega_0 T_i + \psi_i$, P_0, T_i, and ψ_i are the frequency of the optical wave, phase of the optical wave, the power of the optical wave in each branch, the delay of the i^{th} waveguide (before the i^{th} ring modulator), and a constant phase, respectively. The UWB pulse waveform, $p(t)$, impinging from a certain direction, arrives at the i^{th} ring modulator (on the i^{th} branch) with the delay of τ_i (which is set by the angle of incidence). The electric field of the modulated light after the i^{th} modulator is written as

$$E_{M,i}(t) = p(t-\tau_i)\sqrt{P_M}e^{j(\omega_i t+\phi_i)}, \quad \textbf{(S4)}$$

where the modulator is approximated as an electro-optic multiplier. The light at the output of the i^{th} modulator is optically delayed by τ_i' such that output of all four modulators arrive at a certain pixel at the same time, that is, $\tau_i + \tau_i' = \tau_0$ for i =1, 2, 3, 4. In this case, the four modulated optical waves at the combining point are written as

$$E_{DM,i}(t) = p(t-\tau_0)\sqrt{P_{DM}}e^{j(\omega_i' t+\phi_i')}, \quad \textbf{(S5)}$$

where $\omega_i' = \omega_i - 4\pi\alpha\tau_i'$, and $\phi_i' = \phi_i + 2\pi\alpha(\tau_i'^2 + 2\tau_i' T_i) - \omega_0\tau_i' + \theta_i$, P_{DM}, and θ_i are the frequency of the optical wave in each branch at the combining point, the phase of the optical wave in each branch at the combining point, the power of the optical wave in all four branches at the combining point, and the optical constant excess phase at the combining point, respectively. The electric field of the optical wave at the combiner output is written as

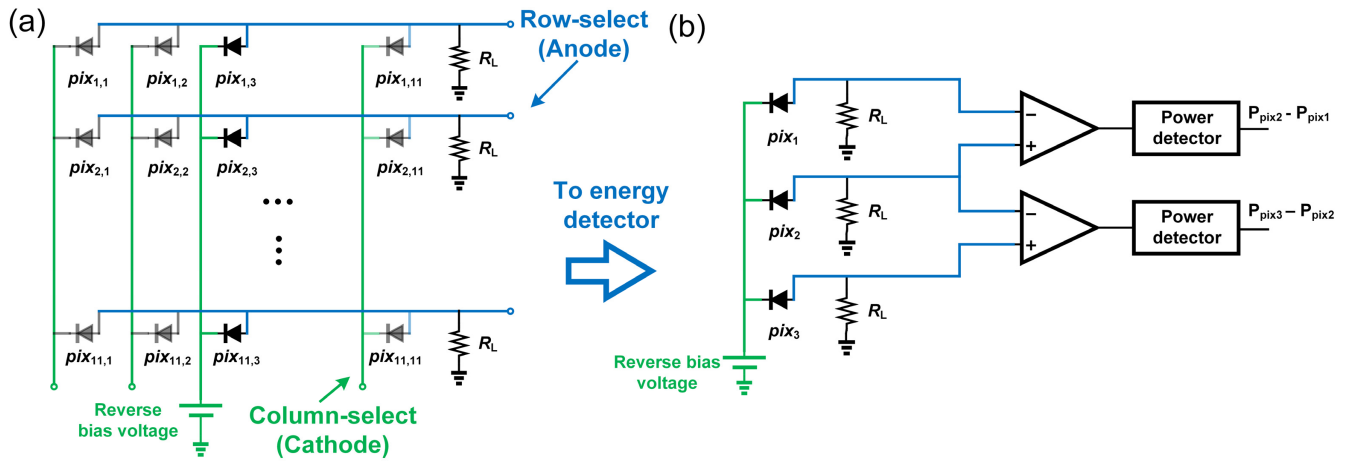

Fig. S6. Data read-out circuitry. (a) Matrix of photodiodes as imager pixels. (b) Differential energy detection circuit.

$$E_{out}(t) = p(t-\tau_0)\sqrt{\frac{P_{DM}}{2}}\sum_{i=1}^{4} e^{j(\omega_i' t+\phi_i')}\, E_{DM,i}(t), \qquad \textbf{(S6)}$$

The output optical wave is photo-detected and the photo-current is written as

$$i_{PD}(t) = RE_{out}E_{out}^{*} = \frac{RP_{DM}}{2}p^2(t-\tau_0)\left\{4 + 2\sum_{\substack{j=1\\ j\neq k}}^{4}\sum_{k=1}^{4}\cos[(\omega_j'-\omega_k')t+\phi_j'-\phi_k')]\right\}, \qquad \textbf{(S7)}$$

where R is the responsivity of the photodiode. The photo-current is amplified and converted to a voltage using a trans-impedance amplifier (TIA) resulting in $v_{out}(t) = Gi_{PD}(t)$, where G is the trans-impedance of the TIA. Finally, a power detector integrates v_{out} to find the output power as

$$P_{out} = (GRP_{DM})^2 P_{p^2}, \qquad \textbf{(S8)}$$

where P_{p^2} is the power of the pulse squared and all cos(.) terms in Equation S7 are averaged to zero during integration. Equation S8 shows that the detected power does not depend on the relative phase between the four modulated optical waves at the combining point. Note that for the pixels that receive only one pulse, Equation S8 is modified to $P_{out} = \frac{1}{4}(GRP_{DM})^2 P_{p^2}$, indicating a factor of four contrast, which is the same as the image contrast in [6].

Figure S5(a) shows the block diagram of the chirp generation system, where the output of a HP-8168F tunable laser is connected to the JDSU 10020484 single-sideband (SSB) modulator after polarization adjustment. The frequency of a Minicircuits ZX95-2500W voltage-controlled oscillator (VCO) is linearly chirped by applying a saw tooth waveform (generated by a Keithley 3390 waveform generator) to its control voltage. The VCO output drives the SSB modulator, chirping the frequency of the tunable laser. The SSB modulator output is amplified to about 30 mW and coupled into the chip. The beat-note between a secondary tunable laser and the SSB modulator output is used to monitor the performance of the SSB modulator. Figures S5(b) and S5(c) show the SSB modulator output spectra with zero biasing and with single-sideband operation biasing, respectively. Under the single-sideband operation condition, the undesired sideband and the optical carrier are significantly suppressed. The frequency of the optical signal is linearly chirped by about 800 MHz over 5 µs.

5. Supplementary Note S5: Data read-out and calibration

The implemented imager consists of 121 pixels as a matrix of 11x11 photodiodes as shown in Fig. S6(a). The current of these photodiodes can be read using a matrix read-out scheme. The anodes of the photodiodes in each row are connected to a row-select line and the cathodes of the photodiodes in each column are connected to a column-select line. By applying a voltage to a column-select line (while keeping the rest of the column-select lines open), the reverse biased current of each of the 11 photodiodes on that column flows though the corresponding row-select line, is converted to a voltage using a resistor (R_L), and power detected. By selecting the columns, one at a time, all 121 photo-currents can be read in 11 steps.

Since pixels are read one column at a time, in principle, 11 power detectors are required to detect the power of the pixels. However, the 11 parallel adjacent lines are highly susceptible to cross-talk and electromagnetic interference, which may result in a poor signal-to-interference ratio making the pixel read-out challenging. To alleviate this issue, a differential power detection scheme is used. Figure S6(b) illustrates the differential power detection circuit (three photodiodes are shown for simplicity), where 10 differential power detectors are used for 11 output channels to detect the relative power between the adjacent photodiodes. To form the image, these relative power measurements are used to estimate the power of each channel during the post-processing phase.

There are three main sources of error in the pixel read-out process that may affect the quality of the image: the cross-talk between the traces of the printed-circuit-board (PCB), the non-uniformity of the optical signal distribution, and the mismatch between the power detectors. The effect of these non-ideal factors is reduced through the calibration process. When both the input laser and the pulse generator are switched off, the power detectors should have a uniform response. However, in practice, the output voltage of the power detectors are not the same. To address this non-uniformity between the power detectors, first the output of the power detectors are measured while the laser and the

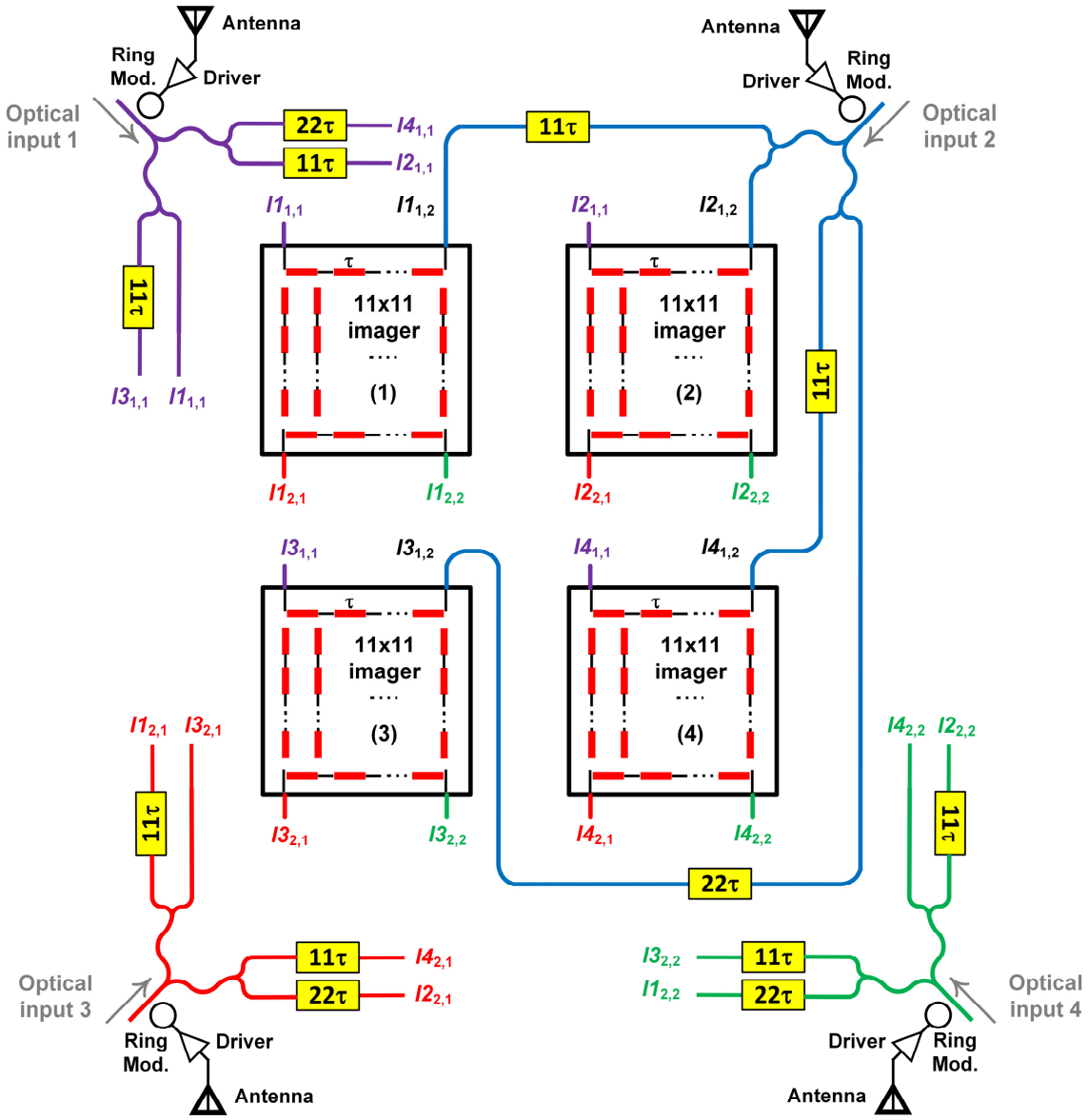

Fig. S7. Scaling the number of pixels by tiling.

pulse generator are off. The image in this case, $I_{\text{light:off/pulse:off}}$, represents the mismatch between the outputs of the power detectors and is referred to as $I_{\text{non-uniform\_P\_detect}}$. To measure the cross-talk between the PCB traces driving the ring modulators and those at the input of the power detectors, the power detector outputs are measured when the laser is off but the pulse generator is on. The result of this measurement, $I_{\text{light:off/pulse:on}}$, represents both the PCB cross-talk and the mismatch between the power detectors. In this case, the image representing the effect of the electrical PCB cross-talk can be calculated as

$$I_{\text{cross-talk}} = I_{\text{light:off/pulse:on}} - I_{\text{light:off/pulse:off}}. \quad \text{(S9)}$$

Ideally, when the input laser is on, all pixels should receive the same amount of optical power. However, in practice, the input optical power may not be equally distributed among all pixels. The image formed for the case that the laser is on but the pulse generator is off, $I_{\text{light:on/pulse:off}}$, represents the effect of both non-uniform optical power distribution and the mismatch between the power detectors. In this case, the image representing the effect of the non-uniform optical power distribution can be calculated as

$$I_{\text{non-uniform dist}} = I_{\text{light:on/pulse:off}} - I_{\text{light:off/pulse:off}}. \quad \text{(S10)}$$

For the final measurement, both the laser and the pulse generator are turned on. In this case, the formed image, $I_{\text{light:on/pulse:on}}$, represents the near-field image of the target object as well as the effect of non-uniform optical power distribution, the cross-talk between PCB traces, and the mismatch between the power detectors, that is,

$$I_{\text{light:on/pulse:on}} = I_{\text{UWB\_image}} + I_{\text{non-uniform dist}} + I_{\text{cross-talk}} + I_{\text{non-uniform\_P\_detect}}. \quad \text{(S11)}$$

Therefore, using Equations S9, S10, and S11, the near-field image of the target object can be calculated as

$$I_{\text{UWB\_image}} = I_{\text{light:on/pulse:on}} - I_{\text{light:on/pulse:off}} - I_{\text{light:off/pulse:on}} + I_{\text{light:off/pulse:off}}. \quad \text{(S12)}$$

Note that for the images shown in Fig. 5(b) of the paper, the three calibration measurements are performed once and the three calibration images are stored and used for image formation.

Supplementary Table S1

Component/equipment	Model
Tunable laser	HP 8168F
Tunable laser (for monitoring)	Agilent 81682B
SSB modulator	JDSU 10020484
EDFA	KEOPSYS KPS-OEM-C-19-WDM
Waveform generator	Keithly 3390
RF spectrum analyzer	HP 8565E
Photodiode/receiver	Multiplex MTRX192L
VCO	Minicircuits ZX95-2500W
RF amplifier (for VCO output)	Minicircuits ZX60-V63+
90° hybrid	Microlab C-45
Pulse generator	AVTECH AVE2-C-5000
Modulator driver pre-amplifier	Minicircuits ZX60-V62+
Ring modulator driver	JDSU H301
Power detector	Analog Devices ADL-5906
Difference amplifier	Analog Devices ADL-5566

6. Supplementary Note S6: Scaling the nanophotonic near-field imager

To increase the number of pixels of the integrated nanophotonic near-field imager, the number of the delay elements in the 1-D array of delay lines in Fig. S2(a) can be increased. In this case, the directional couplers (with varying coupling length and gap), placed between the delay lines, need to be designed to ensure equal power at the output of the directional couplers. For a given minimum feature size of a photonic process, the design of the directional couplers for a delay line array with large number of elements may be challenging since the required coupling length/gap difference between two consecutive directional couplers (to ensure equal output power) may become smaller than the minimum feature size. Alternatively, a practical approach for scaling to a large number of pixels is the tiling scheme, where multiple imagers with smaller pixel counts can be placed next to each other to create an imager with a large number of pixels. Figure S7 illustrates an example of this idea, where four identical 11x11 imagers are placed next to each other to form a 22x22 imager. In this case, the UWB signal received by each antenna is used to modulate the input light using ring modulators. The modulator outputs are guided to all four 11x11 imagers. The modulated light is routed to the closest 11x11 imager with no extra delay. However, to route the same signal to other imagers, extra delays are added to account for the total delay of the closer imagers.

References

1. D. Colton and R. Kress, *Inverse Acoustic and Electromagnetic Scattering Theory* Ch. 2 (Springer, New York, 2013).
2. B. Pile and G. Taylor, "Small-signal analysis of microring resonator modulators," Opt. Express **22**, 14913-14928 (2014).
3. S. Park and S. Jeon, "A 15–40 GHz CMOS true-time delay circuit for UWB multi-antenna systems," IEEE Microw. Wireless Compon. Lett. **23**, 149-151 (2013).
4. T. Chu, J. Roderick, and H. Hashemi, "An integrated ultra-wideband timed array receiver in 0.13 µm CMOS using a path-sharing true Time delay architecture," IEEE J. Solid-State Circuits, **42**, 2834-2850 (2007).
5. J. Roderick, H. Krishnaswamy, K. Newton, and H. Hashemi, "Silicon-based ultra-wideband beam-forming," IEEE J. Solid-State Circuits, **41**, 1726-1739 (2006).
6. T. S. Chu and H. Hashemi, "True-time-delay-based multi-beam arrays," IEEE Trans. Microw. Theory Tech. **61**, 3072-3082 (2013).
7. Z. N. Low, J. H. Cheong, and C. L. Law, "Low-cost PCB antenna for UWB applications," IEEE Antennas Wireless Propag. Lett. **4**, 237-239 (2005).